

# GPU-accelerated Bayesian inference for block-cave mine monitoring via muon tomography

Miguel Biron-Lattes<sup>1</sup>, Patrick Belliveau<sup>2</sup>, Faezeh Yazdi<sup>1</sup>, Samopriya Basu<sup>1</sup>,  
Donald Estep<sup>1</sup>, Derek Bingham<sup>1</sup>, and Doug Schouten<sup>2</sup>

<sup>1</sup>Department of Statistics and Actuarial Science, Simon Fraser University

<sup>2</sup>Ideon Technologies Inc.

April 1, 2026

## Abstract

We describe a Bayesian framework for an inverse problem arising from monitoring block caving operations via muon tomography. We work with a low dimensional surface-based representation of the geometry of the block cave, which dramatically reduces the computational requirements of the model while allowing realistic geometries. Adopting a Bayesian approach, we define a prior distribution on the space of geometries that favors realistic cave shapes. Pairing this prior with a likelihood based on the muon tomography forward model, we obtain a posterior distribution over cave geometries using Bayes rule. We obtain approximate samples from this posterior distribution using Markov chain Monte Carlo algorithms running on GPUs, resulting in fast and accurate sampling. We test the fidelity of our methodology by applying it to a simulated block caving scenario for which the ground truth is known. Results show that our method produces a diverse array of sensible geometries that are simultaneously compatible with the data.

## 1 Introduction

*Block caving* (see e.g. Laubscher, 1994; Chitombo, 2010) refers to a process that involves undermining an ore body and then allowing it to collapse under its own weight. The broken ore falls into funnels built underneath the caving zone, where it is then extracted (left panel in Fig. 1). This technique provides a way to reach large, lower-grade deposits deep underground, achieving high production rates at a fraction of the operating cost and environmental impact of conventional surface mining methods. As such, block cave mining is an effective way to extend the extraction from an ore deposit when the near-surface ore has been depleted.

Accurate and timely spatial information of block cave geometry is critical for efficient ore recovery and maintaining safety (Lett et al., 2016; Flores, 2019;

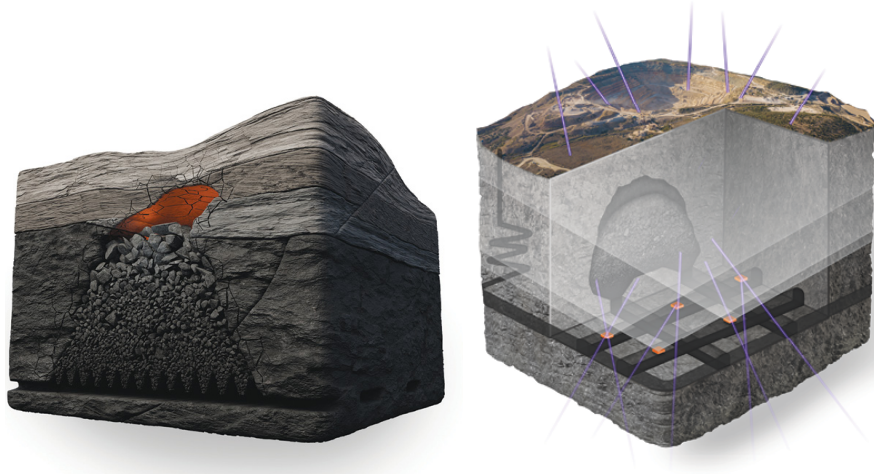


**Figure 1:** Three-dimensional illustration of block caving. **Left:** depiction of the three main units: solid rock, muck pile, and air gap. Funnels that capture broken ore can be seen below the muck pile. **Right:** muons penetrating through the mine, with some intersecting the field of view of sensors placed at the bottom of the cave.

Dawn, 2019). In particular, knowledge of the cave boundaries can help improve safety through monitoring hazardous air gap development, enhance the efficiency of the mine, and increase accuracy of production forecasts. The problem is thus to determine mine geometry using mostly indirect observational data. Current monitoring methods rely on the placement of instrumentation within sparsely distributed drillholes, producing time-series data of the locations of trackers. Therefore, this approach can only provide sparse and localized information about the state of the cave.

In this paper, we consider using *muon tomography* (Tanaka, 2013; Schouten and Ledru, 2018; Bonechi et al., 2020; Bonomi et al., 2020; Schouten et al., 2022) to determine mine geometry. Briefly, cosmic-ray muons are charged elementary particles that arise naturally from cosmic radiation interacting with the Earth’s atmosphere. Particle showers of muons bombard Earth steadily and are attenuated by their interaction with matter along their trajectory. Muons can penetrate deep into the Earth’s crust, down to thousands of meters. Importantly, their attenuation in matter is proportional to the density of material the muon passes through. By measuring the flux of surviving muons using detectors—positioned in drillholes and beneath the surface (right panel in Fig. 1)—the average density along each ray path within a wide field of view above the detector can be determined. Each device produces a radiographic image of the rock mass above it, and combining the images from several devices yields three-dimensional tomographic reconstructions of subsurface density.

Unfortunately, the available data are insufficient to produce a direct image of the geometry of the cave back, muck pile, or air gap. As a result, most of

the cave structure is unknown, including the geometry of any possible air gap. Realizing the full potential of this technology requires solving the inverse problem associated with tomography; namely, inverting from the muon attenuation data to the distribution of mass in the cave. Muon tomography-derived density models have been successfully deployed to monitor block cave propagation remotely (Schouten et al., 2022, 2024). Still, there remain unsolved challenges in the ability to produce a solution that reflects the uncertainty in the geometry.

In this work we develop a Bayesian model for the determination of block caving geometry via muon tomography. Our modeling approach exploits key features of the problem in order to drastically reduce the dimension of the unknown variables representing the geometry, enabling fast evaluation of the resulting forward model. In turn, this allows us to perform inference on this model using state of the art Markov chain Monte Carlo (MCMC; see e.g. Geyer, 1992; Tierney, 1994; Gilks et al., 1995; Brooks et al., 2011) software that leverage the recent increase in availability of Graphic Processing Units (GPUs) designed to accelerate numerical computations (Phan et al., 2019).

To check the fidelity of our proposed methodology, we apply it to a simulated block caving scenario for which the ground truth is known. The simulations show that the MCMC chains converge to the posterior probability distribution on cave geometries. In particular, the samples obtained produce useful risk assessments of the existence of an air gap at the top of the cave. This suggests that our proposed method constitutes a principled and effective approach for muon tomography inversion with strong uncertainty quantification. We finish by discussing potential avenues of research towards improving the models and samplers.

## 2 Methodology

We begin by defining the forward model that relates block cave geometry to muon counts at the detectors. Since we aim to apply MCMC samplers that utilize gradient information for proposal generation (see Section 3), we focus on a version of the computer model that is end-to-end differentiable. Finally, we describe the Bayesian approach to the inverse problem, which involves defining a prior probability distribution over feasible geometries.

### 2.1 Description of the forward model

#### 2.1.1 Low-dimensional representation of the cave geometry

To represent the geometry of a block cave, we choose a surface-based approach, in which the subsurface is represented by the location of the interfaces between the distinct units of which it is comprised. Referring to Fig. 1, we show three distinct units: solid rock, muck pile, and air gap. When the material properties of each unit are known to a high degree, the uncertainty lies in their shape and location. In turn, these can be specified by the location of their interfaces. This approach dramatically reduces the number of variables needed to specify a

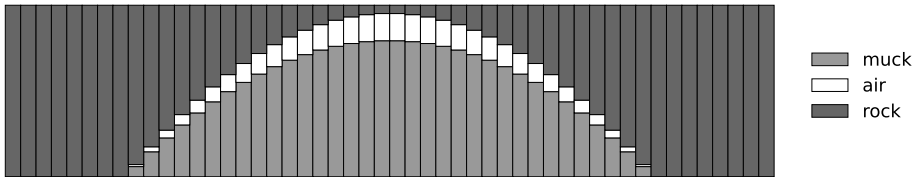


**Figure 2:** A two-dimensional visualization of a layer model with 3 distinct units representing rock, muck pile, and possible air gap.

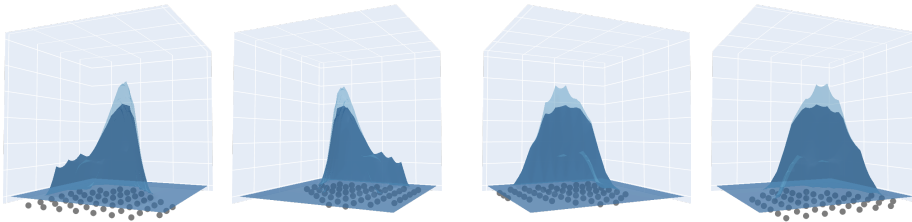


**Figure 3:** Four perspectives of the true layers of the simulated example dataset. Axis labels have been omitted for clarity. Base  $x$ - $y$  grid is of size  $19 \times 19$  with an extent of 760 meters in each direction, while the  $z$  axis has a range of  $(-25, 625)$  meters. The two layers have been plotted with transparency in order to show the non-trivial air gap at the top of the formation, and the location of the muon sensors (at constant  $z = -25$ ).

geometry, as it transforms a three-dimensional problem—the specification of the mass density at every point in the inversion domain—into the two-dimensional issue of finding vertical limits for the interfaces between geological units.

Specifically, we use *layer models* for geological surfaces, consisting of a collection of layers defined on a fixed grid with specified thickness. The layers are arranged sequentially to represent a three-dimensional object. Fig. 2 shows a two-dimensional visualization of a three layer model. This family of models is prevalent in the Earth sciences to represent portions of the subsurface that are known to consist of layered sedimentary strata (see e.g. Webber and van Geuns, 1990; Turner, 2006; Enemark et al., 2022).

Assume the inversion domain  $\mathcal{D}$  has the shape of a box. We discretize the  $x$ - $y$  plane of  $\mathcal{D}$  into a grid of size  $n_{\text{rows}} \times n_{\text{cols}}$ , and divide the box vertically into  $n_{\text{layers}}$  layers. We let  $H_{\ell, x, y} \geq 0$  be the relative height with respect to the floor of  $\mathcal{D}$  of the  $\ell$ -th layer,  $\ell \in \{1, \dots, n_{\text{layers}}\}$ , at the grid point  $(x, y)$ .

In block caving applications, we represent the geometry using 3 layers corresponding to the interfaces between 1) muck pile and air gap; 2) air gap and solid rock, and 3) solid rock and the Earth’s surface. The goal is to perform inference on the thicknesses of the first two layers, since the location of the Earth’s surface is known. Fig. 3 shows the layer model (without the top of the terrain to simplify the visualization) corresponding to a realistic simulated cave model provided by a block-caving expert (Diering, 2023). Note that the first layer is flat except where the muck pile is located. Similarly, the thickness of the air layer is zero everywhere except where the air gap lives. These zero-thickness regions allow

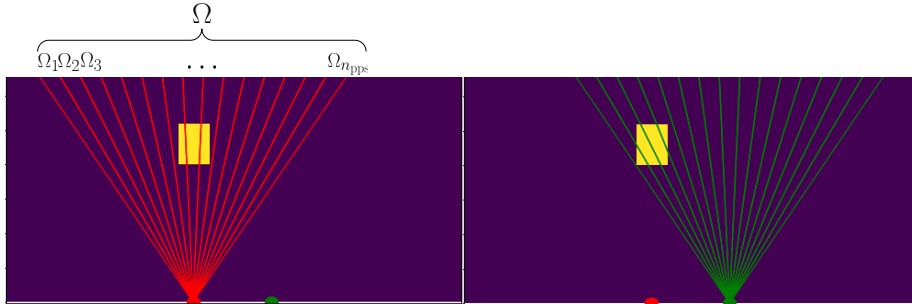


**Figure 4:** Two-dimensional illustration of the field of view of two sensors (semi-circles at the bottom) imaging a rectangular object from two different positions. Rays emanating from a sensor indicate the partition of the field of view into distinct pixels.

layer models to represent realistic geometries while still fundamentally remaining in two-dimensional space—thereby keeping computational costs in check. In practice, we enforce strictly positive thicknesses to avoid numerical issues. This restriction has no practical effect, as thicknesses can be as close to 0 as necessary.

### 2.1.2 Muon attenuation

The forward model for muon tomography estimates the rate of muons arriving at a sensor given a specific instance of a layer model. Muon sensors are placed at known positions in  $\mathcal{D}$  with a given field of view specified by a solid angle  $\Omega$ . This field of view is decomposed into  $n_{\text{pps}}$  pixels per sensor, each with a specific portion  $\Omega_p$  of solid angle so that  $\{\Omega_p\}_{p=1}^{n_{\text{pps}}}$  defines a partition of  $\Omega$ . Fig. 4 shows an illustration.

Given a density field  $\rho : \mathcal{D} \rightarrow [0, \infty)$ , the arrival of muons at each pixel is modeled as a Poisson process conditionally independent of other pixels. Specifically, for any exposure time  $\Delta t > 0$ , the number of muons detected at the  $p$ -th pixel is assumed to follow a Poisson distribution with mean

$$\lambda_p(\rho) := \Delta t \int_{\Omega_p} \mathcal{I}(\mathcal{O}(\rho, \hat{n})) \varepsilon(\hat{n}) d\theta, \quad (1)$$

where

- $\Omega_p$  is the solid angle associated with the  $p$ -th pixel.
- $\mathcal{I}$  is the muon intensity function
- $\hat{n} = \hat{n}(\theta)$  is the normal vector associated to a given  $\theta \in \Omega$ .
- $\varepsilon(\hat{n})$  is the efficiency of the detector as a function of the direction  $\hat{n}$ .
- $\mathcal{O}(\rho, \hat{n}) = \int_{\varrho(\hat{n})} \rho(x(u), y(u), z(u)) du$  is the opacity along the ray  $\varrho(\hat{n})$  that starts at the sensor and has direction  $\hat{n}$ .

$\mathcal{I}$  is determined by the muon source, and  $\varepsilon$  is related to how well the device detects muons incident from the specified direction. We refer the reader to Schouten et al. (2022) for a detailed description of these functions.

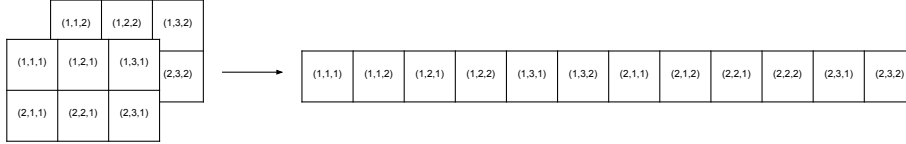


**Figure 5:** An example of reshaping a three-dimensional array of size  $(2, 3, 2)$  into a vector of length 12, using the convention in which the right-most index varies the fastest.

Practical implementations of Eq. (1) employ numerical approximations to the integrals. One approximation is given by piece-wise constant fields defined on a grid. Specifically, we discretize the domain  $\mathcal{D}$  into a regular three-dimensional grid with steps  $(\Delta x, \Delta y, \Delta z)$  and sizes  $(n_x, n_y, n_z)$ —implying a total of  $n_{\text{grid}} = n_x n_y n_z$  grid elements or *voxels*. The discretization along the first two coordinates may match the one used for the layer model, but this is not necessary. We assume that there is a map  $(i, j) \mapsto (x(i), y(j))$  taking the first two density-grid indices into layer-grid indices.

Using the density-grid we represent piecewise constant density fields as three-dimensional arrays  $R$ . It is helpful to view  $R$  as a vector of  $n_{\text{grid}}$  “stacked” voxels (see Fig. 5). Any linear indexing of the array is theoretically valid, but picking the memory layout convention used by the language in which the model is implemented is most efficient as it makes the translation between the two types of indices computationally free. We overload the notation and let  $\lambda_p : \mathbb{R}^{n_{\text{grid}}} \rightarrow \mathbb{R}^+$  be the restriction of Eq. (1) to piece-wise constant density fields defined on the grid.

### 2.1.3 Speeding-up model evaluation through linearization

It is known that the uncertainty quantification benefits of using MCMC for sampling the posterior distribution of an inverse problem can come at a high computational cost, due to the number of model evaluations the method requires (Mosegaard and Tarantola, 1995). While several approaches exist to tackle this issue (Higdon et al., 2003; Christen and Fox, 2005), in this work we opt for a simpler alternative. Leveraging the fact that  $R \mapsto \lambda_p(R)$  is differentiable, we work with a linear approximation around a reference density array  $R_0$ . Consider the first-order Taylor expansion

$$\lambda_p(R) = \lambda_p(R_0) + \frac{\partial \lambda_p}{\partial R}(R_0)^\top (R - R_0) + O(\|R - R_0\|^2), \quad (2)$$

where  $\frac{\partial \lambda_p}{\partial R}(R_0)$  is the gradient of the expected counts evaluated at the reference grid. Stacking Eq. (2) across all  $n_{\text{pps}}$  pixels in all  $n_{\text{sensors}}$  sensors and dropping higher order terms yields a linear approximation to the forward model

$$\hat{\lambda}(R) := \lambda(R_0) + G(R - R_0). \quad (3)$$

Here, both  $\hat{\lambda}(R)$  and  $\lambda(R_0)$  are stacked vectors of  $n_{\text{pixels}} := n_{\text{sensors}} \cdot n_{\text{pps}}$  expected muon counts, while  $G$  is the  $n_{\text{pixels}} \times n_{\text{grid}}$  *sensitivity* matrix built by stacking

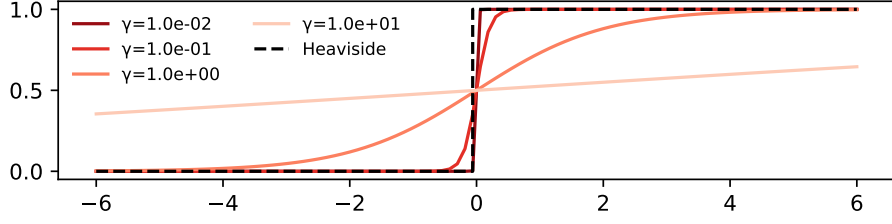


**Figure 6:** Visualization of the approximation of the Heaviside function via scaled sigmoid functions, for different values of the scale parameter  $\gamma$ .

the gradients at every pixel. Note that  $G$  is sparse, as only a handful of grid elements interact with the field of view of a given pixel. Therefore, using sparse linear algebra routines to compute Eq. (3) results in a fast approximation to the expected muon counts.

We stress that the linearization of  $R \mapsto \lambda_p(R)$  does not make the full inverse problem linear, as we still are missing a component model linking cave geometry to a density array. The next section shows that this link is, in fact, highly non-linear.

### 2.1.4 Smoothly mapping layer heights into density grids

The final step in building the forward model approximation is translating a layer model into a density grid. To this end, note that a voxel  $(i, j, k)$  in the grid is below the upper limit of the  $\ell$ -th layer if  $k\Delta z < H_{\ell, x(i), y(j)}$ . It follows that a point in the grid is inside the  $\ell$ -th layer if the previous condition holds and also  $k\Delta z > H_{\ell-1, x(i), y(j)}$  (recall that  $H_{0, x, y} = 0$ ). Since a layer model assumes known densities within each unit—which we can view as fixed arrays  $\{R^{(\ell)}\}_{\ell=1}^{n_{\text{layers}}}$ —the overall density array  $R$  associated with a given layer model  $H$  can be expressed as

$$R_{i,j,k}(H) = \sum_{\ell=1}^{n_{\text{layers}}} [\eta(H_{\ell, x(i), y(j)} - k\Delta z) - \eta(H_{\ell-1, x(i), y(j)} - k\Delta z)] R_{i,j,k}^{(\ell)} \quad (4)$$

where  $\eta : \mathbb{R} \rightarrow \{0, 1\}$  is the Heaviside function, defined as

$$\eta(u) := \begin{cases} 0 & u < 0 \\ 0.5 & u = 0 \\ 1 & \text{o.w.} \end{cases}$$

As we mentioned at the beginning of Section 2, we aim for a differentiable forward model that will allow us to use MCMC algorithms that make use of gradient information. The presence of the Heaviside function breaks this property. Therefore, we replace the Heaviside with a smooth approximation. We employ

the scaled sigmoid (or logistic) function

$$\varsigma_\gamma(u) := \frac{1}{1 + \exp(-u/\gamma)},$$

for some  $\gamma > 0$ . Fig. 6 shows a visualization of the behavior of the function for different  $\gamma$  values. It is easy to check that  $\varsigma_\gamma \rightarrow \eta$  as  $\gamma \rightarrow 0$ .

Choosing a smoother sigmoid increases the computational efficiency at a cost of “smearing” the boundary between material types, increasing uncertainty in the result. Experimentally, we find that values of  $\gamma$  around 1 strike an acceptable balance between the two competing effects. Hence, we set  $\gamma = 1$ , and simplify the notation by writing  $\varsigma = \varsigma_1$ .

Replacing the Heaviside by the sigmoid in the summand of Eq. (4) yields

$$D_{i,j,k}^{(\ell)}(H) := \varsigma(H_{\ell,x(i),y(j)} - k\Delta z) - \varsigma(H_{\ell-1,x(i),y(j)} - k\Delta z). \quad (5)$$

Note that  $D_{i,j,k}^{(\ell)}(H) \in [0, 1]$ , because the first term always dominates the second term, since layers are increasing in height. Plugging these smooth indicators into Eq. (4) gives

$$\sum_{\ell=1}^{n_{\text{layers}}} D_{i,j,k}^{(\ell)}(H) R_{i,j,k}^{(\ell)} \quad (6)$$

Unfortunately,  $\sum_{\ell=1}^{n_{\text{layers}}} D_{i,j,k}^{(\ell)}(H)$  is not guaranteed to be exactly 1, as is the case if we work with the Heaviside function. In other words, the collection of smooth indicators defined by Eq. (5) is not a partition of unity. Thus, Eq. (6) may produce density values that lie outside of the range specified by the known density fields  $\{R_{i,j,k}^{(\ell)}\}_{\ell=1}^{n_{\text{layers}}}$ , and therefore are not physically meaningful. We correct Eq. (6) using the normalization

$$\hat{R}_{i,j,k}(H) := \sum_{\ell=1}^{n_{\text{layers}}} W_{i,j,k}^{(\ell)}(H) R_{i,j,k}^{(\ell)}, \quad W_{i,j,k}^{(\ell)}(H) := \frac{D_{i,j,k}^{(\ell)}(H)}{\sum_{\ell'=1}^{n_{\text{layers}}} D_{i,j,k}^{(\ell')}(H)}, \quad (7)$$

where the weights  $W_{i,j,k}^{(\ell)}(H)$  now define a partition of unity. Substituting Eq. (7) into Eq. (3) then yields a smooth approximation  $\lambda(\hat{R}(H))$  to the expected muon count function.

## 2.2 Bayesian calibration

The preceding sections described the forward model of muon tomography, where a known geometry is used to compute the expected number of muons that would be measured by a collection of detectors. We now turn our attention to the inverse problem, where the goal is to recover the geometry given muon counts  $\{C_p\}_{p=1}^{n_{\text{pixels}}}$  at every pixel. As mentioned in Section 2.1.2, these data are

inherently stochastic and, conditional on the layer heights  $H$ , follow a Poisson distribution

$$C_p | H \stackrel{\text{indep}}{\sim} \text{Poisson}(\lambda_p(\hat{R}(H))). \quad (8)$$

In this work, we use a Bayesian approach for inferring layer heights. In this framework (see e.g. Mosegaard and Tarantola, 1995; Kennedy and O’Hagan, 2001; Lee et al., 2002; Kaipio and Somersalo, 2005), Eq. (8) corresponds to the *likelihood*, defining a probability distribution of the data conditional on the unknown parameters. The forward model is an intrinsic part of the likelihood, as it gives the “typical” data that is expected for a specific realization of the parameters. In the context of this paper, the forward model defines the expected muon counts for a given geometry. The second component in the Bayesian formulation corresponds to the *prior* distribution, which encapsulates *a priori* knowledge about the unknown parameters. The following section describes a novel prior probability distribution for layer models.

After gathering field observations, we update our knowledge about the unknown parameters using Bayes’ theorem to obtain a *posterior* probability distribution over the unknowns. Conceptually, Bayes’ theorem reads

$$\text{posterior} = \frac{\text{prior} \times \text{likelihood}}{\text{marginal likelihood}}.$$

The *marginal likelihood* (also known as *evidence*) is a normalization constant that ensures the posterior is a probability measure. Although hard to compute in general (Friel and Wyse, 2012; Fourment et al., 2019), MCMC can be used even if this quantity is unknown, as these algorithms typically only require computing ratios of posterior density (Tierney, 1994). We will discuss the algorithms we employ to sample from the posterior distribution in Section 3.

### 2.2.1 Constructing a prior for layer models

The key of the Bayesian approach is choosing an adequate prior. In this section we focus on defining a prior distribution for layer heights. We begin with a model that, at grid location  $(x, y)$ , assigns the height of the base layer  $H_{1,x,y}$  by sampling uniformly from the available space  $[0, H_{n_{\text{layers}},x,y}]$ . By sampling iteratively conditional on the previous layers, we choose the height of the  $\ell$ -th layer uniformly from the remaining space  $[H_{\ell-1,x,y}, H_{n_{\text{layers}},x,y}]$ . Mathematically,

$$\begin{aligned} H_{1,x,y} &\stackrel{\text{indep}}{\sim} \text{Unif}(0, H_{n_{\text{layers}},x,y}) \\ H_{\ell,x,y} | H_{\ell-1,x,y} &\stackrel{\text{indep}}{\sim} \text{Unif}(H_{\ell-1,x,y}, H_{n_{\text{layers}},x,y}), \quad \ell \in \{2, \dots, n_{\text{layers}} - 1\}, \end{aligned} \quad (9)$$

where  $\text{Unif}(a, b)$  is the uniform distribution on the interval  $[a, b]$ . Note that we can use any distribution with support on a finite interval. We use the uniform prior as a non-informative choice since, *a priori*, we do not know where the boundaries of these geological units lay.

It is clear that the model in Eq. (9) satisfies the height constraints: layers are placed sequentially in order from bottom to top, and they all reside inside the enclosing boundaries. However, the model has an important drawback, since it essentially defines a collection of *independent columns* (if  $(x_1, y_1) \neq (x_2, y_2)$ , the random vectors  $H_{\cdot, x_1, y_1}$  and  $H_{\cdot, x_2, y_2}$  are independent). This allows for very rough surfaces that are not physically possible, which is especially problematic when the data are scarce and weakly informative.

One way to introduce spatial structure between columns to Eq. (9) starts by noting that it can be re-written as

$$\begin{aligned} u_{\ell, x, y} &\stackrel{\text{iid}}{\sim} \text{Unif}(0, 1) \\ H_{1, x, y} &= (1 - u_{1, x, y}) \cdot 0 + u_{1, x, y} H_{n_{\text{layers}}, x, y} \\ H_{\ell, x, y} &= (1 - u_{\ell, x, y}) H_{\ell-1, x, y} + u_{\ell, x, y} H_{n_{\text{layers}}, x, y}, \quad \ell \in \{2, \dots, n_{\text{layers}}\}. \end{aligned}$$

To allow for within-layer dependence between the heights at different grid points, we substitute the i.i.d. collection  $\{u_{\ell, x, y}\}_{x, y}$  with another  $\{\tilde{u}_{\ell, x, y}\}_{x, y}$  that maintains the marginal  $\text{Unif}(0, 1)$  distributions but has non-trivial dependence. To this end, *copulas* (Joe, 2014) provide a framework for modeling dependence among collections of random variables while maintaining their marginal distributions. Perhaps the simplest copula is the Gaussian. To obtain the collection of dependent uniform variates, we first simulate a multivariate normal  $\mathcal{N}(0, \Sigma)$  in  $\mathbb{R}^{n_{\text{rows}} \cdot n_{\text{cols}}}$  with prescribed covariance matrix  $\Sigma$ , and then apply an element-wise cumulative distribution function (c.d.f.) transformation to obtain correlated  $\text{Unif}(0, 1)$  random variables (see e.g. Owen, 2013, Example 5.9).

Thus, we have translated the problem of drawing spatially dependent uniform random variables to sampling from a multivariate normal distribution. It remains to define an appropriate correlation structure for the layers. For layer models, the graph defined by the nearest neighbors to every grid element provides a natural undirected graph structure. To this end, conditional autoregressive processes (CAR, Besag, 1974; see also Rue and Held, 2005, Section 2.2) provide a convenient parametrization of multivariate normal distributions on arbitrary graphs  $G = (V, E)$ , where  $V$  is a set of vertices and  $E$  a set of edges, assuming the graphs contains no self-loops (i.e.,  $(i, i) \notin E$  for any  $i \in V$ ). CAR processes are specified from the *full conditional distributions*: if  $x \in \mathbb{R}^{|V|}$ —with  $|V|$  the number of nodes in the graph—is a sample from a CAR process, then  $x$  follows a multivariate normal distribution satisfying

$$\mathbb{E}[x_i | x_{-i}] = - \sum_{j \in V: j \sim i} \phi_{i, j} x_j, \quad \text{Var}(x_i | x_{-i}) = \kappa_i^{-1}, \quad (10)$$

where  $x_{-i} = \{x_j : j \neq i\}$ ;  $i \sim j$  means  $(i, j) \in E$ ;  $\phi$  is a matrix of coefficients, and  $\kappa$  is a vector of conditional inverse variances or *precisions*. Thus, we see that a CAR process is specified through the influence that neighborhoods have on vertices. A pair  $(\kappa, \phi)$  yields a valid CAR process specification if the *precision matrix*

$$Q = \text{diag}(\kappa)(I + \phi)$$

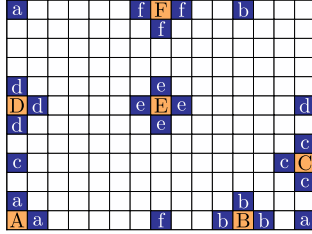


**Figure 7:** Visualization of the neighbors (blue) of selected nodes (yellow) in the nearest-neighbor graph of a  $12 \times 15$  grid assuming a periodic domain. We denote the different selected nodes with capital letters, whereas their respective neighbors are marked with the corresponding lower-case symbol. Notice how the neighborhoods of some nodes wrap around the edges.

is positive definite, where  $\text{diag}(v)$  is the diagonal matrix with diagonal equal to the vector  $v$ . In this case,  $x \sim \mathcal{N}(0, \Sigma)$ , where  $\Sigma = Q^{-1}$  is the covariance matrix.

We define the *adjacency matrix*  $A$  of the graph  $(V, E)$ , that has entries

$$A_{i,j} = \begin{cases} 1 & i \sim j \\ 0 & \text{otherwise.} \end{cases}$$

A simple non-trivial valid CAR process defined on the graph uses (Gelfand and Vounatsou, 2003, Section 3)

$$\kappa = A\mathbf{1}, \quad \phi = -r \text{diag}(\kappa^{-1})A,$$

where  $\mathbf{1} = (1, \dots, 1) \in \mathbb{R}^{|V|}$ , and  $r \in [0, 1)$  is a spatial dependence parameter. Using these expressions in Eq. (10), we see that this CAR process establishes positive correlation between nodes and its neighbors, while it forces nodes with larger neighborhoods to have lower variance. Specifically, the nodes are independent when  $r = 0$ , whereas they become increasingly more correlated as  $r \rightarrow 1$ . The precision matrix in this case simplifies to

$$Q = \text{diag}(A\mathbf{1}) - rA, \tag{11}$$

which is positive-definite for  $r \in [0, 1)$ . For many graphs of interest,  $A$  is a sparse matrix, since every node is connected to only a handful of neighbors, which in turn means that  $Q$  is sparse. As we shall soon see, this can be computationally advantageous (Rue, 2001).

Specifying a member of this family of CAR processes thus requires selecting a specific graph structure and a scalar  $r \in [0, 1)$ . As we said before, we use the nearest-neighbor graph induced by the layer grid. We further impose a periodic boundary condition, as illustrated in Fig. 7. Doing so has the effect of making all the node neighborhoods of the same size (4), which in turn means that all the coordinates of the CAR process have the same marginal distribution.

We treat the spatial correlation as a hierarchical parameter to be learned from data. We assume *a priori* independent per-layer spatial dependency parameters

$\{r_\ell\}_{\ell=1}^{n_{\text{layers}}}$  distributed as

$$r_\ell \stackrel{\text{i.i.d.}}{\sim} \text{Unif}(0, 1).$$

We choose this distribution because it is non-informative, as in general we do not have *a priori* knowledge of the strength of spatial association. However, more informative distributions supported on  $(0, 1)$ —such as specific choices of the Beta distribution—may be used whenever such knowledge is available.

It remains to specify a procedure to simulate from the CAR process. We start from a fundamental property of multivariate normal distributions. If  $z \sim \mathcal{N}(0, I)$  is a vector of i.i.d. standard normal variables, and if there is a matrix  $U$  such that  $\Sigma = UU^\top$ , then  $x = Uz$  follows a  $\mathcal{N}(0, \Sigma)$  distribution. To leverage this approach, let  $L$  be a Cholesky factorization of the precision matrix in Eq. (11); i.e., a lower-triangular matrix such that  $Q = LL^\top$ . As we mentioned before, the sparseness of  $Q$  may make this procedure more efficient if sparse linear algebra routines are available. In any case, consider the identity

$$\Sigma = Q^{-1} = (LL^\top)^{-1} = (L^\top)^{-1}L^{-1} = (L^{-1})^\top L^{-1} = UU^\top,$$

where  $U := (L^{-1})^\top$  is upper-triangular and can be computed efficiently. It follows that if  $z \sim \mathcal{N}(0, I)$ ,  $x := Uz$  is a sample from  $\mathcal{N}(0, \Sigma)$  and therefore from the CAR process.

With the CAR sample available, we obtain a collection of correlated  $\text{Unif}(0, 1)$  random variables via the c.d.f. transform

$$\check{u}_i := \Phi\left(\frac{x_i}{\sqrt{\Sigma_{i,i}}}\right) = \Phi\left(\frac{x_i}{\sqrt{(UU^\top)_{i,i}}}\right) = \Phi\left(\frac{x_i}{\sqrt{\sum_j U_{i,j}U_{j,i}}}\right),$$

where  $\Phi : \mathbb{R} \rightarrow (0, 1)$  is the c.d.f. of the standard normal distribution.

### 3 Experimental setup

As discussed earlier, we use MCMC to sample from the posterior distribution given by the computer model, the observed muon counts, and the prior. Here we detail the specific algorithms used and the software involved in the implementation.

#### 3.1 Markov chain Monte Carlo sampling algorithms

Given the nature of the model at hand, we expect to encounter challenges in the sampling process due to high correlation in the posterior distribution. These difficulties stem from the fact that the height of one layer cannot be changed without altering at least one other layer, so that the total height of the layer model remains the same. Therefore, samplers that ignore these induced correlations will take a prohibitively long time to converge. We thus require

advanced MCMC samplers that take into account the posterior geometry when proposing moves. In order to have access to such advanced MCMC samplers, we implement the model in NumPyro (Phan et al., 2019), a Python-based probabilistic programming language (PPL; see e.g. Rainforth, 2017 and van de Meent et al., 2018). PPLs allow researchers to write large classes of probabilistic models in a common language, and provide implementations of state of the art MCMC samplers that can run off-the-shelf on any such model. Compared to other PPLs, NumPyro has the additional benefit of being written in JAX (Bradbury et al., 2018), a Python framework with Numpy-like syntax that allows for automatic differentiation, vectorization, and just-in-time compilation that produces efficient code for both CPUs and GPUs. Thus, NumPyro allows us to take advantage of the recent increase in availability of compute-oriented GPUs with no additional coding effort.

Automatic differentiation enables the use of state of the art gradient-based samplers that produce high-quality posterior samples with manageable cost, like Hamiltonian (or Hybrid) Monte Carlo (HMC, Duane et al., 1987; see also Neal, 2011; Betancourt, 2018). Let us call *latent vector* the result of reshaping (as in Fig. 5) and stacking all the unknown variables in the model into a single one-dimensional array. Roughly speaking, HMC identifies the latent vector with the position of a fictitious particle, which it associates with a momentum variable. By carefully designing an energy function in phase space, the trajectories given by exactly integrating Hamilton’s equations interspersed with random momentum perturbations produce (correlated) samples from the target distribution.

In practice, however, numerical integration is required to solve for HMC trajectories, which in turn forces the introduction of an accept-reject step in order to compensate for the loss of accuracy. The integrator has two parameters: a positive step size, and the number of steps to take at each iteration. Finding adequate values for these parameters is a hard problem. In our experiments we use the no-u-turn sampler (NUTS) introduced in Hoffman and Gelman (2014), an adaptive version of HMC. At each iteration, NUTS finds an adequate number of integration steps to take so as to avoid backtracking by stopping after encountering a so called *u-turns*. Backtracking arises due to the fact that, under mild conditions, the constant-energy orbits of the Hamiltonian system are periodic. Therefore, the process returns to its initial state in finite time. By identifying the point at which the distance to the origin starts to decrease—i.e., a u-turn—NUTS stops integrating past that point to avoid wasting computational resources, resulting in an overall more efficient sampler. Additionally, NUTS defines a robust adaptation procedure to tune the step size parameter.

### 3.2 Multiple independent chains via vectorization

We take advantage of automatic vectorization to run several chains simultaneously on the same GPU. Running independent chains with random initializations is an easy way to improve the exploration of the posterior distribution. To avoid performance degradation of the vectorized sampler caused by MCMC steps with widely varying random duration (see e.g. Dance et al., 2025)—which are common

when employing adaptive samplers such as NUTS—we lower the maximum trajectory length that NUTS is allowed to evaluate to the lowest possible value that does not result in sample quality degradation. We find that a maximum trajectory of 256 steps strikes a good balance. In this regime, almost all NUTS iterations reach the maximum trajectory length—and therefore take roughly the same time to complete—resulting in little to no degradation of the vectorized sampler.

Notwithstanding the above, naively running independent chains with arbitrary initialization can give the impression of mixing when in fact each chain ends up stuck in a subset of the state space dictated entirely by the (arbitrary) initial state. In order to detect the presence and severity of this effect, we follow the simulation design introduced by Margossian et al. (2024), where  $n_{\text{chains}} := n_{\text{super}} \cdot n_{\text{within}}$  chains are grouped into  $n_{\text{super}}$  *super-chains*, each with  $n_{\text{within}}$  components. Every super-chain is assigned a randomly sampled initial state, and all its  $n_{\text{within}}$  component chains start from this state. Such experimental design allows us to detect convergence issues. Indeed, in an ideal setting, every chain is able to explore the full posterior distribution, regardless of their initial state. Therefore, samples from different super-chains should be indistinguishable. In the opposite case, chains are stuck in a neighborhood close to their starting point, and thus samples from different super-chains look nothing alike. The authors provide the nested- $\hat{R}$  diagnostic—a generalization of the standard  $\hat{R}$  or Gelman–Rubin diagnostic (Gelman and Rubin, 1992)—that aims to quantify these behaviors, based on a simple decomposition of the variance of the samples.

For the experiments in the next section, we use  $n_{\text{super}} = 32$  super-chains, assigning each to a different GPU that run  $n_{\text{within}} = 8$  chains in a vectorized fashion. This strikes a reasonable balance between resource constraints and sample quality. Each chain is ran for  $2^{15}$  adaptation steps—during which the step size of the integrator is automatically tuned—followed by  $2^{12}$  sampling steps. Moreover, following the suggestions in Margossian et al. (2024), we discard as warm-up (or burn-in) all but the last of these samples, leaving a total of  $n_{\text{chains}} = 256$  independent samples approximately distributed according to the posterior. This has negligible impact on the sample quality—due to the presence of high auto-correlation—but it makes sampling considerably faster, as it avoids the (slow) transfer of samples between GPU and host memory. Finally, we note that if an application required increased precision and thus additional independent samples, the ideal way to produce them is by running more super-chains while keeping the rest of the configurations above fixed.

## 4 Simulation experiment

As we described in Section 2, the block-caving example visualized in Fig. 3 corresponds to a simulated cave model, which means we have access to the true heights  $H^{\text{true}}$ . In particular, we can compute the expected counts under this geometry  $\lambda(\hat{R}(H^{\text{true}}))$ . By rounding these values to the nearest integer and

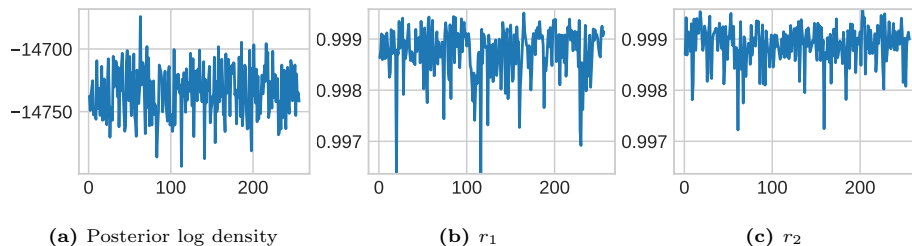


**Figure 8:** Visualization of samples corresponding to the last step of all the 256 chains. Samples from the same super-chain are plotted contiguously. **Left to right:** Values for the (unnormalized) posterior log density (a), and the hierarchical parameters  $r_1$  (b) and  $r_2$  (c).

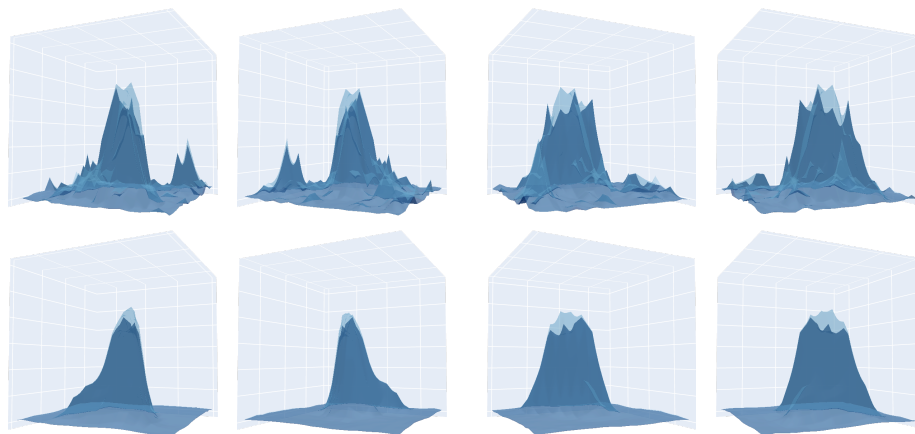


**Figure 9:** Four perspectives on two point estimators for the layer heights. **Top:** sample with the highest posterior density (MAP). **Bottom:** posterior mean of the layer heights.

treating them as experimental counts, we can empirically assess if our proposed framework is able to produce samples that are compatible with  $H^{\text{true}}$ .

Fig. 8 shows traces for the (un-normalized) posterior log density and the spatial correlation parameters  $(r_1, r_2)$ . Values from the same super-chain are plotted contiguously. The fact these groups are not visually noticeable in the trace of the posterior log-density (Fig. 8a) suggests adequate mixing. Indeed, traces look like independent samples from the same distribution. We corroborate this by calculating the nested- $\hat{R}$  diagnostic for all latent variables. The worst (i.e., highest) value across all dimensions is 1.12, which is close to the ideal of 1, implying that no obvious convergence issue is present.

We also notice in Figs. 8b and 8c that all the chains show layer smoothness values  $(r_1, r_2)$  close to 1, indicating that the sampled geometries evidence spatial dependence. This validates the modeling choice of replacing the independent columns prior with structured layers, as described in Section 2.2.1.

Fig. 9 shows a visualization of two point estimates of the cave geometry: the

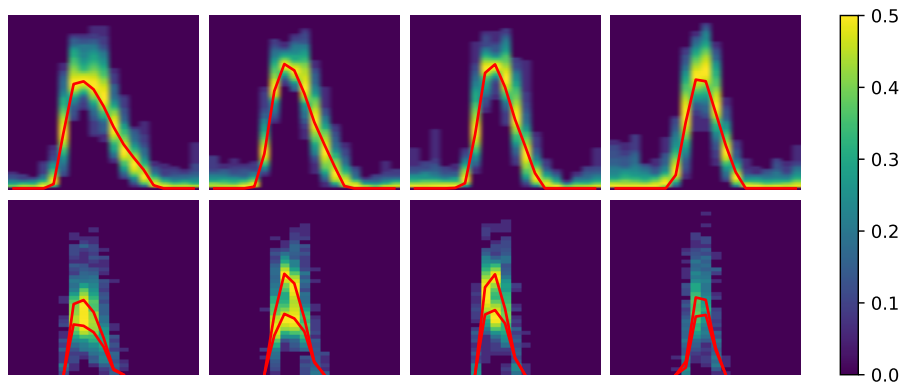


**Figure 10:** Tomographic visualization across four selected slices along the  $y$  axis, showing the standard deviation across samples of layer indicators (Eq. (5)), as a way to visualize uncertainty in the predicted boundaries. Red lines correspond to true interfaces. **Top:** cave-rock interface. **Bottom:** both air gap boundaries (muck and rock), zooming-in on the top of the cave to aid visualization.

sample estimate of the maximum *a posteriori* (MAP)—i.e., the sample with the highest posterior density—and the posterior mean of the layer heights (or, equivalently, the thicknesses, as these are related by a linear transformation). The MAP looks like a noisy version of the true geometry, such that its overall shape and features are recovered. The spikiness of the MAP evidences the uncertainty in the exact position of the layers. We expect this uncertainty to be higher in regions with no sensors, as evidenced by the fictitious secondary cave shown in the first two plots of the top row of Fig. 9. On the other hand, the posterior mean averages out this type of noise, resulting in a geometry that is closer to the truth than any specific sample.

Still, the volume of air seems under estimated in both summaries shown in Fig. 9. In contrast to such point estimates, adequate risk assessment should also provide uncertainty estimates. To this end, Fig. 10 shows a tomographic visualization of the uncertainty in the predicted layer locations, across four selected slices along the  $y$  axis of the domain  $\mathcal{D}$ . Specifically, the heat maps show the standard deviation across samples of layer indicators (Eq. (5)). The metric is contained in  $[0, 0.5]$ , where 0 indicates full confidence in the value of the layer indicator, while 0.5 corresponds to maximal uncertainty. The latter case indicates the probable locations of the layer interfaces. Thus, we overlay the images with the true layer boundaries in order to assess the effectiveness of the methodology. The top row of Fig. 10 focuses on the cave-rock interface, where we see that the likely boundary locations are consistent with the ground truth. The bottom row presents the two boundaries of the air gap—muck pile below and rock above—again showing a high level of agreement with the truth.

## 5 Conclusions

In this work we described a Bayesian model for muon tomography, along with a procedure for performing inference via MCMC. We described how our implementation leveraged recently developed computational frameworks that simplify the description of the model, offer off-the-shelf state-of-the-art samplers, and allow seamless execution of the inference process on GPUs. We study the properties of our method in a simulated block caving dataset, where the true geometry is known. These experiments suggest that our proposed MCMC scheme is able to adequately explore the space of geometries defined by our parametrization of the problem. In particular, these simulations suggest that the methodology is able to capture the risk of air gap at the top of the cave.

The results suggest several potential avenues of future research. On the computational side, we note that the bottleneck of our model lays in the matrix manipulations required to simulate layers of correlated heights. In the future, it would be interesting to consider alternative specifications of the underlying Gaussian random fields and/or of simulation techniques which might speed-up the evaluation of the posterior density. In terms of the modeling approach, it is important to note that layer models cannot express the totality of cave geometries that can arise (e.g., hourglass-shaped). In the future, we would like to explore the use of level sets to describe more complex geometries (see e.g. Xie et al., 2011; Iglesias et al., 2016).

## Acknowledgments

The authors wish to thank Tony Diering for kindly providing us with the simulated block caving example we use throughout this work. Derek Bingham acknowledges the support of the Natural Sciences and Engineering Research Council of Canada. Donald Estep’s work has been partially supported by the Canada Research Chairs Program, the Natural Sciences and Engineering Research Council of Canada, Canada’s Digital Technology Supercluster, the Dynamics Research Corporation, the Idaho National Laboratory, the United States Department of Energy, the United States National Institutes of Health, the United States National Science Foundation, and Riverside Research.

## Code availability

A GitHub repository has been set up for the algorithms and Python code developed in this work: <https://github.com/Estep-Bingham-Lab/layermodels-repr>.

## References

- Besag, J. (1974). “Spatial interaction and the statistical analysis of lattice systems.” *Journal of the Royal Statistical Society: Series B (Methodological)*, 36(2): 192–225.
- Betancourt, M. (2018). “A conceptual introduction to Hamiltonian Monte Carlo.” *arXiv e-prints*, arXiv:1701.02434.
- Bonechi, L., D’Alessandro, R., and Giammanco, A. (2020). “Atmospheric muons as an imaging tool.” *Reviews in Physics*, 5: 100038.
- Bonomi, G., Checchia, P., D’Errico, M., Pagano, D., and Saracino, G. (2020). “Applications of cosmic-ray muons.” *Progress in Particle and Nuclear Physics*, 112: 103768.
- Bradbury, J., Frostig, R., Hawkins, P., Johnson, M. J., Leary, C., Maclaurin, D., Necula, G., Paszke, A., VanderPlas, J., Wanderman-Milne, S., and Zhang, Q. (2018). “JAX: composable transformations of Python+NumPy programs.” URL <http://github.com/jax-ml/jax>
- Brooks, S., Gelman, A., Jones, G., and Meng, X.-L. (2011). *Handbook of Markov chain Monte Carlo*. CRC press.
- Chitombo, G. P. (2010). “Cave mining: 16 years after Laubscher’s 1994 paper ‘Cave mining—state of the art’.” *Mining Technology*, 119(3): 132–141.
- Christen, J. A. and Fox, C. (2005). “Markov chain Monte Carlo using an approximation.” *Journal of Computational and Graphical Statistics*, 14(4): 795–810.
- Dance, H., Glaser, P., Orbanz, P., and Adams, R. P. (2025). “Efficiently vectorized MCMC on modern accelerators.” In Singh, A., Fazel, M., Hsu, D., Lacoste-Julien, S., Berkenkamp, F., Maharaj, T., Wagstaff, K., and Zhu, J. (eds.), *Proceedings of the 42nd International Conference on Machine Learning*, volume 267 of *Proceedings of Machine Learning Research*, 12436–12458. PMLR.
- Dawn, T. (2019). “Technologies of ground support monitoring in block caving operations.” In Hadjigeorgiou, J. and Hudyma, M. (eds.), *Ground Support 2019: Proceedings of the Ninth International Symposium on Ground Support in Mining and Underground Construction*, 109–122. Australian Centre for Geomechanics.
- Diering, T. (2023). “DeepCove.” Personal communication.
- Duane, S., Kennedy, A., Pendleton, B. J., and Roweth, D. (1987). “Hybrid Monte Carlo.” *Physics Letters B*, 195(2): 216–222.

- Enemark, T., Andersen, L. T., Høyer, A.-S., Jensen, K. H., Kidmose, J., Sander-  
sen, P. B., and Sonnenborg, T. O. (2022). “The influence of layer and voxel  
geological modelling strategy on groundwater modelling results.” *Hydrogeology  
Journal*, 30(2): 617–635.
- Flores, G. (2019). “Major hazards associated with cave mining—are they  
manageable?” In *Proceedings of the First International Conference on Mining  
Geomechanical Risk, Australian Centre for Geomechanics, Perth*, 31–46.
- Fourment, M., Magee, A., Whidden, C., Bilge, A., Matsen, F., and Minin, V.  
(2019). “19 dubious ways to compute the marginal likelihood of a phylogenetic  
tree topology.” *Systematic Biology*, 69(2): 209–220.
- Friel, N. and Wyse, J. (2012). “Estimating the evidence—a review.” *Statistica  
Neerlandica*, 66(3): 288–308.
- Gelfand, A. E. and Vounatsou, P. (2003). “Proper multivariate conditional  
autoregressive models for spatial data analysis.” *Biostatistics*, 4(1): 11–15.
- Gelman, A. and Rubin, D. B. (1992). “Inference from iterative simulation using  
multiple sequences.” *Statistical Science*, 7(4): 457 – 472.
- Geyer, C. J. (1992). “Practical Markov chain Monte Carlo.” *Statistical Science*,  
7(4): 473–483.
- Gilks, W. R., Richardson, S., and Spiegelhalter, D. (1995). *Markov chain Monte  
Carlo in practice*. CRC press.
- Higdon, D., Lee, H., and Holloman, C. (2003). “Markov chain Monte Carlo-based  
approaches for inference in computationally intensive inverse problems.” In  
Lindley, V., Bernardo, J. M., Bayarri, M. J., Berger, J. O., Dawid, A. P.,  
Heckerman, D., Smith, A. F., and West, M. (eds.), *Bayesian Statistics 7: Pro-  
ceedings of the Seventh Valencia International Meeting*, 181. Oxford University  
Press.
- Hoffman, M. D. and Gelman, A. (2014). “The No-U-Turn Sampler: Adaptively  
setting path lengths in Hamiltonian Monte Carlo.” *The Journal of Machine  
Learning Research*, 15(1): 1593–1623.
- Iglesias, M. A., Lu, Y., and Stuart, A. M. (2016). “A Bayesian level set method for  
geometric inverse problems.” *Interfaces and Free Boundaries*, 18(2): 181–217.
- Joe, H. (2014). *Dependence modeling with copulas*. Chapman and Hall/CRC.
- Kaipio, J. P. and Somersalo, E. (2005). *Statistical and computational inverse  
problems*. Springer.
- Kennedy, M. C. and O’Hagan, A. (2001). “Bayesian calibration of computer  
models.” *Journal of the Royal Statistical Society: Series B (Statistical Method-  
ology)*, 63(3): 425–464.

- Laubscher, D. (1994). “Cave mining—the state of the art.” *Journal of the Southern African Institute of Mining and Metallurgy*, 94(10): 279–293.
- Lee, H. K., Higdon, D. M., Bi, Z., Ferreira, M. A., and West, M. (2002). “Markov random field models for high-dimensional parameters in simulations of fluid flow in porous media.” *Technometrics*, 44(3): 230–241.
- Lett, J., Jäger, A., Thornhill, T., Rachocki, J., Mobilio, B., Carr, C., and Chitombo, G. (2016). “Geotechnical challenges in cave monitoring—a modern approach.” In *Proceedings Seventh International Conference and Exhibition on Mass Mining (MassMin 2016)*, 203–216. The Australasian Institute of Mining and Metallurgy.
- Margossian, C. C., Hoffman, M. D., Sountsov, P., Riou-Durand, L., Vehtari, A., and Gelman, A. (2024). “Nested  $\hat{R}$ : Assessing the convergence of Markov chain Monte Carlo when running many short chains.” *Bayesian Analysis*, 1 – 28.
- Mosegaard, K. and Tarantola, A. (1995). “Monte Carlo sampling of solutions to inverse problems.” *Journal of Geophysical Research: Solid Earth*, 100(B7): 12431–12447.
- Neal, R. (2011). “MCMC using Hamiltonian dynamics.” In Brooks, S., Gelman, A., Jones, G., and Meng, X.-L. (eds.), *Handbook of Markov chain Monte Carlo*, chapter 5, 47–95. CRC Press.
- Owen, A. B. (2013). *Monte Carlo theory, methods and examples*. <https://artowen.su.domains/mc/>.
- Phan, D., Pradhan, N., and Jankowiak, M. (2019). “Composable effects for flexible and accelerated probabilistic programming in NumPyro.” *arXiv:1912.11554*.
- Rainforth, T. (2017). “Automating inference, learning, and design using probabilistic programming.” Ph.D. thesis, University of Oxford.
- Rue, H. (2001). “Fast sampling of Gaussian Markov random fields.” *Journal of the Royal Statistical Society: Series B (Statistical Methodology)*, 63(2): 325–338.
- Rue, H. and Held, L. (2005). *Gaussian Markov random fields: Theory and applications*. Chapman and Hall/CRC.
- Schouten, D., Furseth, D., and van Nieuwkoop, J. (2022). “Muon tomography for underground resources.” In Oláh, L., Tanaka, H. K., and Varga, D. (eds.), *Muography: Exploring Earth’s subsurface with elementary particles*, chapter 16, 221–235. American Geophysical Union and John Wiley and Sons, Inc.
- Schouten, D. and Ledru, P. (2018). “Muon tomography applied to a dense uranium deposit at the McArthur river mine.” *Journal of Geophysical Research: Solid Earth*, 123(10): 8637–8652.

- Schouten, D., Phillips, N., and Merrill, R. (2024). “Cosmic-ray muon tomography.” In Johansson, D. and Schunnesson, H. (eds.), *MassMin 2024: Proceedings of the International Conference & Exhibition on Mass Mining*, 1576–1583. Luleå University of Technology.
- Tanaka, H. K. (2013). “Subsurface density mapping of the earth with cosmic ray muons.” *Nuclear Physics B*, 243: 239–248.
- Tierney, L. (1994). “Markov chains for exploring posterior distributions.” *The Annals of Statistics*, 22(4): 1701–1728.
- Turner, A. K. (2006). “Challenges and trends for geological modelling and visualisation.” *Bulletin of Engineering Geology and the Environment*, 65(2): 109–127.
- van de Meent, J.-W., Paige, B., Yang, H., and Wood, F. (2018). “An introduction to probabilistic programming.” *arXiv:1809.10756*.
- Webber, K. and van Geuns, L. (1990). “Framework for constructing elastic reservoir simulation models.” *Journal of Petroleum Technology*, 42(10): 1248–1297.
- Xie, J., Efendiev, Y., and Datta-Gupta, A. (2011). “Uncertainty quantification in history matching of channelized reservoirs using Markov chain level set approaches.” In *SPE Reservoir Simulation Conference*, SPE–141811.